International Journal of Heat and Mass Transfer 256 (2026) 127972

Contents lists available at ScienceDirect

International Journal of Heat and Mass Transfer

journal homepage: www.elsevier.com/locate/hmt

Development and validation of a full-interface numerical model for determining contact heat transfer coefficients at rough metallic interfaces

Tim Göttlich *, Mustafa Çavdır, Thorsten Helmig, Reinhold Kneer

Institute of Heat and Mass Transfer (WSA), RWTH Aachen University, Augustinerbach 6, 52056 Aachen, Germany

ARTICLE INFO

Keywords:
Thermal Contact Conductance
Contact heat transfer
Inverse heat transfer
3D heat conduction

ABSTRACT

For the precise determination of the temperature distribution in technical systems using thermal modeling, the selected boundary conditions are crucial for the quality of the results. Especially at the contact surface between two components, thermal contact resistance plays a significant role in heat transfer within multicomponent systems. Although extensive experimental work has identified various factors influencing contact heat transfer, deriving universally applicable analytical models remains challenging due to the simplified assumptions made to represent complex surface geometries. In this work, a surface-resolved full-interface numerical model is presented to model the contact heat transfer coefficient between two contacting surfaces and their associated bodies. The numerical temperature profiles for three different sample pairings with varying surface structures are compared to experimental data from infrared thermography. A good agreement is observed for both the temperatures and the estimated contact heat transfer coefficients. The advantage of this surface-resolved approach is that it captures microscopic resistance due to roughness and macroscopic resistance due to long-wavelength form within a single integrated simulation, avoiding separate multiscale treatments and keeping computational effort acceptable.

1. Introduction

Proper thermal management of systems during the design process is essential for the safe and efficient operation of technical systems while maintaining the specified maximum temperatures of individual components, such as electric motors or lithium-ion batteries [1,2]. Thermal modeling is an effective tool for determining the occurring heat flows and the resulting temperature fields within the system. However, the choice of boundary conditions is essential to model reality as accurately as possible. In technical multi-component systems, the interfaces between the components are of particular importance. At these contact surfaces between the bodies, the microscopic roughness caused by the production process results in a restriction of the heat flow and an associated temperature drop. This can be described using the contact heat transfer coefficient h_c, which is defined as the ratio between heat flux $\dot{Q}$ flowing over the nominal contact area A_{nom} and the resulting temperature drop ΔT_c.

$$h_c = \frac{\dot{Q}}{A_{nom}\Delta T_c} \tag{1}$$

In various experimental studies, the influence of different variables, such as the surface topology [3], the contact pressure [4], certain material parameters like surface hardness [5] and thermal conductivity of the contact partners [6], the temperature level [7] and the interstitial medium [8] in the cavities was investigated. In order to describe the contact heat transfer coefficient analytically, the various influencing variables of the problem are divided into three sub-problems: geometry, mechanics and heat transfer [9]. An initial analytical correlation to describe the contact heat transfer coefficient was developed by Cooper et al. [10] and later enhanced by Mikić [11]. This can be determined as a function of the geometric parameters regarding standard deviation of profile height σ and mean of absolute slope m of the surfaces, the mechanical parameters regarding surface hardness H and contact pressure p and the thermal parameter regarding thermal conductivity λ.

$$h_c = 1.13 \cdot \lambda \cdot \frac{m}{\sigma} \cdot \left(\frac{p}{p+H}\right)^{0.94} \tag{2}$$

To simplify the calculation, an isotropic surface with a Gaussian height distribution is assumed and real surfaces are mapped using simplified description parameters. However, technical surfaces do not always fulfill these assumptions, which often results in the analytical correlation overestimating the resulting contact ratio A_{real}/A_{nom} due to a homogeneous distribution of the contact points and thus also overestimating the contact heat transfer coefficient. These simplified

* Corresponding author.
E-mail address: goettlich@wsa.rwth-aachen.de (T. Göttlich).

https://doi.org/10.1016/j.ijheatmasstransfer.2025.127972
Received 29 April 2025; Received in revised form 26 September 2025; Accepted 14 October 2025
Available online 24 October 2025

analytical approaches are therefore well suited for an initial estimation of the contact heat transfer coefficient. However, for an exact estimation of the contact heat transfer without making simplifying assumptions, the contact area and the heat transfer phenomena that occur must be resolved in more detail using numerical simulations. Murashov and Panin [12] have developed a numerical approach based on the finite element method to investigate the influence of strain hardening during elastic–plastic deformation on the contact heat transfer, using generated fractal surfaces with dimensions $90 \times 90\,\mu m$. The surface roughness could be resolved very accurately as only a very small representative section of a conformal contact was simulated. An et al. [13] investigated the influence of the surface topology for conformal contact on the microscopic contact heat transfer using an FEM model based on generated fractal surfaces with dimensions of $125 \times 125\,\mu m$. However, Bahrami [14] emphasizes that it is necessary to consider not only the microscopic unevenness due to roughness but also the macroscopic unevenness due to shape changes on the contact heat transfer. However, the length scales of the macroscopic unevenness cannot be mapped if only a small representative part of the entire surface is simulated. To address this, Thompsen [15] developed an iterative multiscale model based on the finite element method, in which he simulated the contact surfaces at macro level and then resolved a measured representative contact surface at micro level together with its roughness. The contact heat transfer coefficient determined in this way was then provided to the macro simulation as a boundary condition. In order to determine the contact heat transfer of real, optically measured fractal surfaces, Frekers et al. [16] developed a numerical methodology consisting of a mechanical contact simulation that simulates a surface segment of $2 \times 2\,mm$ and a subsequent thermal simulation to map the near-surface temperature field in a section of $2 \times 2\,mm \times 400\,\mu m$. This method accurately captures the microscopic contact resistance but, due to the small simulation domain, cannot account for the macroscopic resistance arising from the overall surface form. To accurately predict heat transfer in real, non-conforming contacts, both resistances must be considered together. The primary novelty of this work, therefore, lies in extending this modeling methodology to resolve the entire surface, including its macroscopic form deviations, within a single, computationally efficient simulation. Unlike traditional multi-scale approaches that treat micro- and macro-scale resistances separately, the model described in this paper directly simulates the combined thermal resistance. This allows for a detailed, high-resolution validation against experimental temperature fields obtained via infrared thermography, demonstrating the model's robustness for predicting heat transfer across real, complex contact interfaces.

2. Experiment

In order to validate the surface-resolved full-interface numerical model, the numerical results must be compared with experimental results. For this purpose, an infrared camera is used to record the resulting surface temperature fields of two contacting samples that are pressed against each other with a defined pressure using a materials testing machine. The detailed description of the experiment is given in the following.

2.1. Samples

The tested surfaces measure a base area of 20 × 20 mm and are the upper surface of a cuboid with a height of 60 mm. The samples are made of AISI 1045 steel, the material properties of which are shown in Table 2. The test surface of the samples is given its final surface structure by the manufacturing process selected in each case. For this purpose, there are three different sample pairings, which differ both in their microscopic roughness and in their macroscopic shape due to their manufacturing parameters. The aim was to produce sample pairings with different surface structures in order to investigate the validity of the model for different surfaces. The surfaces of sample pairing no. 1 were glass bead blasted while the surfaces of sample pairing no. 2 and 3 were milled with different manufacturing parameters. The resulting surfaces of the three tested sample pairings are shown in Fig. 1. It can be seen that the two surfaces of sample pairing no. 1 are nominally parallel and have a randomly distributed, isotropic height distribution. The milled sample surfaces of sample pairings no. 2 and 3, on the other hand, have a structured surface and a macroscopic unevenness. In addition, the surface parameters of the surfaces are shown in Table 1. Here it can be seen that, for example, the mean of absolute slope of the surfaces of pairing no. 1 and 2 is very similar, although the surfaces look different. This emphasizes further that it is very difficult to describe an entire surface geometrically using just a few parameters.

Table 1
Surface parameters of the top and bottom test surfaces for the three sample pairings: mean absolute slope m and standard deviation of profile height σ.

Parameter	no. 1		no. 2		no. 3	
	top	bot	top	bot	top	bot
m [–]	0.11	0.11	0.12	0.13	0.02	0.12
σ [µm]	10.33	10.05	18.43	19.20	0.82	23.24

2.2. Experimental setup

Accurate mounting is essential so that the specimen contact faces are as flat and mutually aligned as in the simulation. Manufacturing tolerances are compensated using shims. Pressure-sensitive films that discolor under load are used to map the contact-pressure distribution. The resulting color maps are compared with the predicted pressure field, and the setup is adjusted until satisfactory agreement is achieved. This ensures that the geometric boundary conditions in the experiment and simulation are the same. As a plausibility check the resulting measured temperature field is compared to the simulation results.

The experimental setup used mainly corresponds to that of Burghold et al. [17,18]. A schematic representation is shown in Fig. 2. The test rig consists of a servo-hydraulic compression testing machine that applies the test load on the samples. The applied force is recorded by a strain gauge. The two samples are clamped in clamping devices that are attached to the machine table and the movable hydraulic cylinder. To ensure consistency with the simulation, the specimens are mounted so that their contact faces are flat and mutually aligned. Manufacturing-induced misalignment is compensated using shims. Pressure-sensitive films that discolor under load are used to visualize the contact-pressure distribution at the contact interface. The observed color maps are compared with the mechanical simulation, and the setup is adjusted as needed until acceptable agreement is achieved. This alignment procedure is performed at a reference contact pressure of 16 MPa. Subsequent measurements at higher pressure levels are performed with the same alignment without readjustment, ensuring that the geometric boundary conditions remain consistent between experiment and simulation.

Cartridge heaters are installed in the upper fixture, which preheat the upper sample to a temperature of 125 °C before the test begins, while the lower sample is set to a temperature of 30 °C. At the beginning of the test, the two samples are pressed together with their respective test surfaces and the test load is applied. The pressure is kept constant during each test. In total, a pressure of 16 up to 48 MPa is tested in the test series. The resulting surface temperature field of the samples is recorded 50 s after the initial contact of the two samples, allowing the temperature equalization process to reach a quasi-stationary state, characterized by linear temperature profiles in the solids at some distance from the contact point. The contact heat transfer coefficient is determined from the measurement data using an inverse analysis, following the methodology introduced by Burghold et al. [17,18]. This analysis utilizes a 10 s interval of the transient measurement, recorded

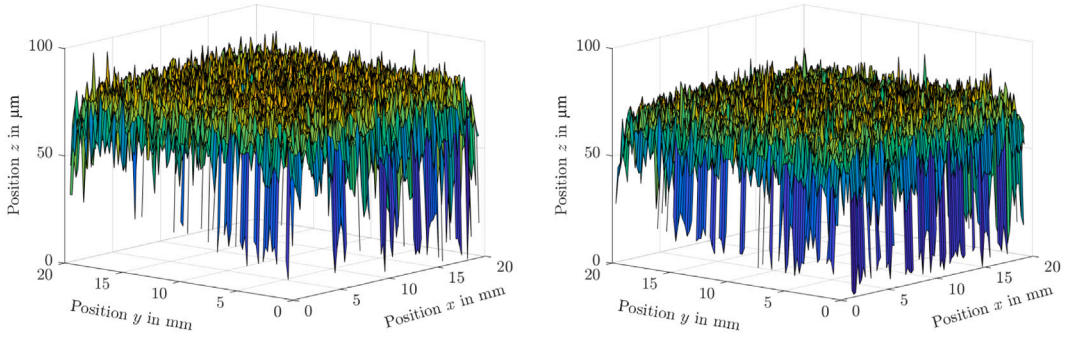

(a) Pairing No. 1.

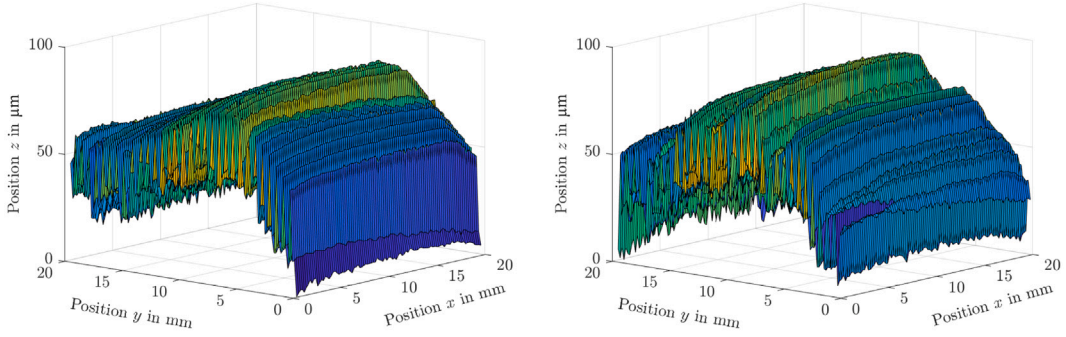

(b) Pairing No. 2.

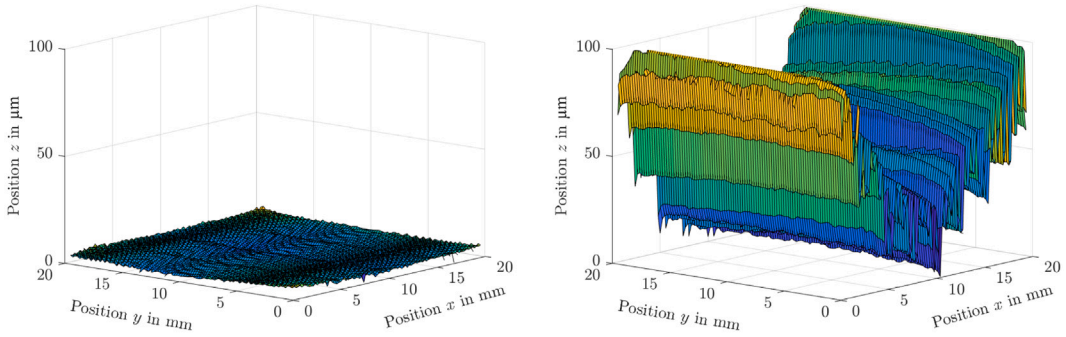

(c) Pairing No. 3.

Fig. 1. Three-dimensional scans of the upper (left) and lower (right) test surface of the three sample pairings, where colors indicate the height of the structure.

from 50 to 60 s after the initial contact. While the overall process is dynamic, the system exhibits quasi-steady-state behavior in this window, which provides a robust basis for the inverse evaluation [19,20].

An Infratec ImageIR 5300 infrared camera is used to measure the temperature fields. It measures in a wavelength range of 3.7 to 4.8 µm and offers an image resolution of 320 × 256 pixels with a pixel size of 210 µm. For the analysis, approximately 100 × 240 pixels of this resolution are utilized. The surface temperature of both samples can thus be observed up to 25 mm away from the contact plane. This area is called "measuring surface" and is coated with a black paint with an emissivity of $\epsilon = 0.975$ to minimize ambient reflections. For the evaluation of the experiment and the subsequent comparison with the simulation, the surface temperature fields of the respective measurement are first averaged over the width in x-direction, which leads to a 1D surface temperature distribution perpendicular to the contact plane. As a boundary condition in the simulation the temperature at a distance of 25 mm from the contact plane is used.

The experimental setup is designed to ensure predominantly one-dimensional heat transport in the axial direction. Although the samples are not fully insulated, the influence of radial heat losses is minimal. For the steel samples (thermal conductivity $\lambda = 51.8\,\mathrm{W/(m\,K)}$) with a cross-section of $20 \times 20\,\mathrm{mm}^2$, a total heat loss coefficient from the sides is assumed to be $10\,\mathrm{W/(m^2\,K)}$. This value is estimated based on typical correlations for natural convection and radiation, considering an averaged sample surface at 65 °C and ambient air at 20 °C. With this heat loss coefficient, the Biot number is calculated as $\mathrm{Bi} = \frac{h_{\mathrm{loss}} L_c}{\lambda} \approx 0.000965$, where L_c is the characteristic length (Volume/Area). Since $\mathrm{Bi} \ll 1$, temperature gradients within the cross-section are negligible, validating the 1D assumption within the bulk material. Nevertheless, the numerical model explicitly accounts for these 3D heat transport phenomena by implementing the side losses as boundary conditions.

2.3. Uncertainty analysis

As the contact heat transfer coefficient h_c is obtained by inverse optimization, its uncertainty is evaluated by perturbing input data and model parameters and re-solving the inverse problem. The dominant input uncertainties are infrared temperature noise (NETD, per-pixel standard deviation $\sigma_{\mathrm{NETD}} = 0.5\,\mathrm{K}$) and the emissivity of the coated measurement surfaces of the specimens, with $\epsilon = 0.975$ and $\sigma_\epsilon = 0.01$. In the inverse evaluation, thermophysical properties are used as model inputs. The thermal diffusivity a combines thermal conductivity λ,

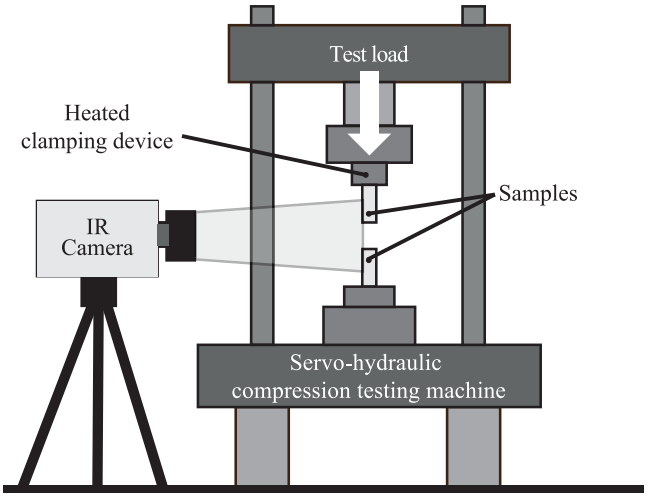

Fig. 2. Schematic of the experimental setup, showing the upper and lower samples, clamping devices, and the field of view of the infrared camera. *Source:* Adapted from Burghold et al. [17].

Table 2
Material properties of AISI 1045 steel.

Property	Symbol	Value
Thermal conductivity	λ	51.8 W/(m K)
Thermal diffusivity	a	13.92 mm^2/s
Young's modulus	E	210 GPa
Poisson's ratio	ν	0.3
Hardness	H	2200 MPa

density ρ, and specific heat c_p ($a = \lambda/(\rho c_p)$) and thus serves as the material input for the estimation of h_c. A relative standard uncertainty of 2% is assumed for a ($\sigma_a/a = 0.02$), which corresponds to $a = 13.92 \pm 0.28\,\text{mm}^2/\text{s}$ in this study.

The influence of these uncertainties on the estimated contact heat transfer coefficient h_c is evaluated using an inverse Monte Carlo analysis [21]. In each Monte Carlo replicate, the emissivity used in the radiometric conversion is treated as a truncated normal (Gaussian) variable with mean 0.975 and standard deviation 0.01 and is bounded to [0.85, 0.999]. Per-pixel NETD noise is modeled as zero-mean Gaussian with a standard deviation of 0.5 K and is added to the infrared temperature field. The thermal diffusivity a is modeled as Gaussian with mean $13.92\,\text{mm}^2/\text{s}$ and standard deviation $0.28\,\text{mm}^2/\text{s}$. Unless stated otherwise, perturbations are sampled independently. For each pressure level and for both pairings, $N = 50$ independent replicates are computed. Expanded uncertainties are reported as $U = 2s$ with coverage factor $k = 2$, which corresponds to approximately 95 % coverage.

3. Numerical model

3.1. Geometry

The first step in modeling is the geometric description of the contact. It is therefore essential to be able to describe the two touching surfaces as accurately as possible. For this purpose, real surfaces of manufactured samples are scanned using a white light interferometer. The entire nominal contact area of 20×20 mm is captured and used directly in the model. The three-dimensional surface scans are represented in a two-dimensional matrix as a function of the x and y coordinates, where each entry corresponds to the respective surface height $z(x, y)$, forming half-space geometries. By accurately mapping the entire surface, it is possible to map both microscopic and macroscopic irregularities on the surface. For the subsequent modeling of contact heat transfer,

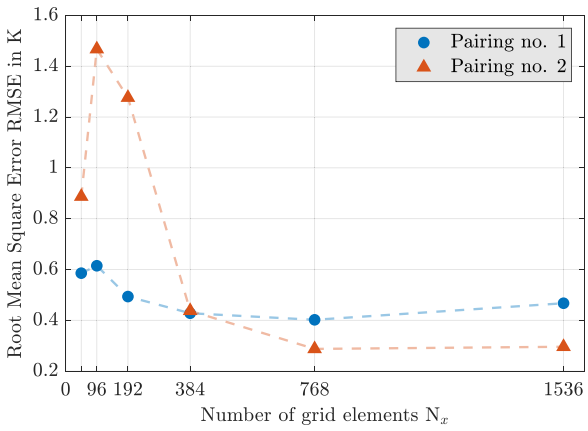

Fig. 3. Comparison of RMSE of measured and calculated temperature profiles as a function of number of grid elements N_x for two sample pairings (p=16 MPa, y=0 mm).

the required resolution of the surfaces is first assessed to minimize the computational effort while keeping computing time and memory requirements within acceptable limits. For this purpose, the Root Mean Square Error (RMSE) of the resulting temperature profile on the measuring surface is presented in a grid study for sample pairing no. 1 and no. 2 at a contact pressure of 16 MPa as a function of the respective grid points in the x–y direction N_x in comparison to the measurement shown in Fig. 3.

It can be observed that the temperature RMSE curves for the two pairings show initially quite different levels, with the RMSE for pairing no. 1 (isotropic) being less affected by improved grid resolution. However, for pairing no. 2 (structured) a clear reduction of the RMSE is found for an increased grid resolution. At a resolution of $N_x = 768$, the RMSE between simulation and measurement is approximately 0.4 K for pairing no. 1 and 0.29 K for pairing no. 2, respectively. These values are relatively small compared to the occurring temperature levels in the experiment. Therefore, a surface resolution of 768×768 cells is considered appropriate for the scope of this work, which corresponds to $\Delta x = \Delta y = 26\,\mu\text{m}$. Although this does not allow for resolving the finest surface structures, it seems to be sufficiently precise for accurately mapping the temperature profile.

3.2. Mechanical modeling

A surface-resolved full-interface half-space contact model with elastic–plastic deformation is used for the mechanics. In this mechanical modeling, only the elastic and plastic deformation of the surfaces is considered and not the entire body as in a three-dimensional FEM. The advantage of this method lies in its emphasis on surface behavior, which is crucial for understanding the contact mechanics. As a result, the surface can be resolved with greater detail, allowing for more efficient use of computational resources by avoiding unnecessary complexity in the solid body. However, it is important to note that this model is limited to capturing normal forces and linear deformations along the z-axis, excluding tangential forces or moments from consideration. The framework of the mechanical modeling is primarily based on the work of Goerke and Willner [22] and Beyer [23].

Using the mechanical model, the corresponding contact pressure is calculated from the deformation of the touching surface points of the two surfaces. To determine the contact points, the distance between the center planes of the top $z_{\text{top}}(x, y)$ and bottom surface $z_{\text{bot}}(x, y)$ is described by the mean separation length δ. Reducing this distance causes an increasing number of surface points to overlap and come into contact. In this modeling approach, the two surfaces are combined into one surface profile and later broken down into the individual surfaces

again. To determine the overlap of the surfaces $u_z(x, y)$, the combined surface is pressed against another flat, rigid surface by the specified distance δ.

$$u_z(x, y) = \left(z_{\text{top}}(x, y) + z_{\text{bot}}(x, y)\right) - \delta \tag{3}$$

All positive entries of $u_z(x, y)$ represent contact points between the two surfaces, while there is no contact at the negative entries and they are set to 0.

For purely elastic deformation $u_{z,\text{el}}(x, y)$, the resulting contact pressure field p can be determined with the rigidity matrix C:

$$u_{z,\text{el}}(x_k, y_k) = \sum_{l=1}^{N_x^2} C_{kl} \cdot p(x_l, y_l) \tag{4}$$

This rigidity matrix C describes the elastic displacement of each surface element (x_l, y_l) with the dimensions of $2\alpha \times 2\beta$, which results from the pressure on another single surface point $p(x_k, y_k)$ as a function of the equivalent modulus of elasticity E^*.

$$C_{kl} = \frac{1}{\pi E^*} \cdot \int_{-\alpha}^{\alpha} \int_{-\beta}^{\beta} \frac{1}{\sqrt{(x_k - x_l - \xi)^2 + (y_k - y_l - \eta)^2}} \mathrm{d}\eta \mathrm{d}\xi \tag{5}$$

This can be determined from the modulus of elasticity E and the Poisson ratio ν of the two surfaces:

$$E^* = \left(\frac{1 - \nu_{\text{top}}^2}{E_{\text{top}}} + \frac{1 - \nu_{\text{bot}}^2}{E_{\text{bot}}} \right)^{-1} \tag{6}$$

However, since only the total surface overlap $u_z(x, y)$ can be determined iteratively using Eq. (3), the elastic deformation $u_{z,\text{el}}$ is replaced by u_z and thus the pressure profile is determined. The resulting system of linear equations is solved using the Gauss–Seidel method with a solver tolerance of 1e-10.

$$p(x, y) = C^{-1} \cdot u_z(x, y) \tag{7}$$

In order to improve the computational performance so that larger surfaces can also be calculated with a high resolution, the active set strategy is implemented [24]. This allows the linear system of equations to be reduced by only calculating the pressure field $p(x, y)$ at the points where contact actually occurs and no longer the entire surface, which significantly reduces the required matrix size. The elastic deformation of the surface is restricted to a local pressure ranging from $p(x, y)$=0 (compressive forces only) to $p(x, y) = H$, with H representing the microhardness of the material. As soon as the local pressure exceeds the microhardness H, plastic deformation occurs, which no longer prevents further deformation. The microhardness H at the surface of the materials can be calculated according to Hencky [25] using the yield strength σ_y of the material.

$$0 \leq p(x_l, y_l) \leq H = 2.8 \cdot \sigma_y \tag{8}$$

The pressure field $p(x, y)$ determined with the help of the total deformation u_z can be used in the next step to calculate the elastic deformation $u_{z,\text{el}}$ using Eq. (4). Finally, the resulting plastic deformation $u_{z,\text{pl}}$ of the surface can then be determined using the difference between the known total overlap u_z and the elastic deformation $u_{z,\text{el}}$.

$$u_{z,\text{pl}}(x, y) = u_z(x, y) - u_{z,\text{el}}(x, y) \tag{9}$$

After determining the total deformation of the combined surface for the specified contact pressure of the combined surface, it has to be partitioned between the two individual surfaces. By using the definition of the elastic strain of the surface, the elastic displacement $u_{z,\text{el}}$ of the two surfaces can be determined as a function of the material properties [26].

$$\frac{u_{z_{\text{top}},\text{el}} \cdot E_{\text{top}}}{1 - \nu_{\text{top}}^2} = \frac{u_{z_{\text{bot}},\text{el}} \cdot E_{\text{bot}}}{1 - \nu_{\text{bot}}^2} \tag{10}$$

The second equation required for the partition is that the total elastic deformation must be equal to the sum of the elastic deformations of the individual surfaces.

$$u_{z,\text{el}} = u_{z_{\text{top}},\text{el}} + u_{z_{\text{bot}},\text{el}} \tag{11}$$

3.3. Thermal modeling

Following the mechanical modeling of the contact to determine the contact geometry, a thermal simulation is set up to determine the resulting temperature field of the samples in contact. For this purpose, the deformed surfaces are modeled with the corresponding base bodies in a three-dimensional model, requiring the solution of the stationary three-dimensional heat conduction equation:

$$0 = \lambda \frac{\partial^2 T}{\partial x^2} + \lambda \frac{\partial^2 T}{\partial y^2} + \lambda \frac{\partial^2 T}{\partial z^2} \tag{12}$$

For the numerical solution, the equation is discretized using the finite volume method. To do this, the computational domain of the sample bodies is structured into a block-structured computational grid. The grid of the thermal simulation is discretized in the x–y expansion with the same cell size as the mechanical simulation. To select the required x–y resolution, a grid study is carried out using sample pairing no. 1. The resulting calculated temperature field at the front of the sample is then compared with the measured one and the root mean squared error (RMSE) is calculated. For this purpose, a mechanical simulation with a subsequent thermal simulation is carried out for the respective x–y resolution. The results are shown in Fig. 3. It can be seen that the RMSE at a resolution of 768 × 768 cells is approx. 0.4 K and that the change in the RMSE also decreases significantly with the number of grid points. Based on this comparison of the surface temperature profile, the chosen resolution of 768 × 768 cells is considered appropriate for the scope of this work and for accurately mapping the temperature profile both at the surface and throughout the bulk material, which corresponds to $\Delta x = \Delta y = 26\,\mu\text{m}$. Although this does not allow for resolving the finest surface structures, it is sufficiently precise for accurately mapping the temperature profile on the measuring surface.

In a second grid study, the sensitivity of the cell size in the z-direction at the boundary near the contact plane is investigated. The results indicate that $\Delta z = 3\,\mu\text{m}$ is a suitable value for the smallest cells in the contact plane between the samples. As shown in Fig. 4(b), this cell size is consistently applied in the regions of the rough surfaces. Moving away from the contact plane, the cell size in z-direction increases by a factor of 2, meaning that each cell in the z-direction is always twice as large as its predecessor. This allows the total number of cells to be significantly reduced and the calculation time to be shortened without affecting the quality of the numerical result. The resulting calculation grid for the thermal simulation is shown in Fig. 4(a) for the front outer surface of the sample bodies.

No additional thermal resistance is taken into account at the solid contact point between a cell of the upper and lower sample, but rather pure thermal conduction in the solids. This simplification is consistent with foundational analytical approaches in contact heat transfer, such as those by Cooper et al. [10] and Mikić [11]. Since the cavities between the two surfaces in the experiment are filled with air, pure thermal conduction through the air is also assumed there. A conservative estimation for the experimental conditions representing the maximum observed temperature difference (interface temperatures of approximately 75 °C for the upper and 55 °C for the lower sample) shows that the contribution of radiation to the total heat flux is below 0.1%. This confirms that neglecting radiation does not introduce a significant source of error for the temperature range considered in this study. For the solution of the heat conduction equation, the boundary conditions at the top and bottom of the sample bodies are selected as constant temperatures, which are read from the experiment. For the outer surfaces of the bodies, a heat loss to the environment $h_{\text{loss}} = 10\,\text{W}/(\text{m}^2\,\text{K})$ due to natural convection and radiation is modeled, where the ambient air has a constant temperature of $T_{\text{amb}} = 20\,°\text{C}$. Finally, a solver based on the conjugate gradients with a solver tolerance of 1e-10 is selected to solve the system of equations.

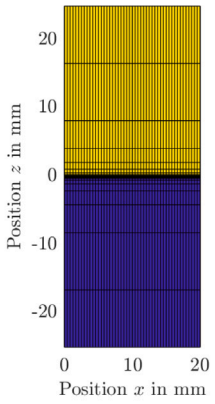

(a) View of the entire grid of the thermal simulation.

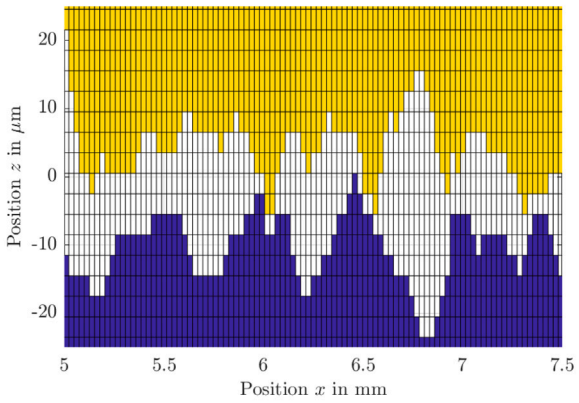

(b) Close-up of the grid of the thermal simulation near the contact.

Fig. 4. Thermal simulation grid for pairing no. 1 at $y = 10\,\text{mm}$ and $p = 16\,\text{MPa}$, where yellow represents the upper sample, dark blue the lower sample and white the ambient air.

4. Validation

In order to validate the surface-resolved full-interface numerical model, the temperature profiles of the experiment and simulation of the different sample pairings on the front observation plane of the infrared camera are first compared with each other. Fig. 5 shows the results for sample pairing no. 1, which has isotropic, glass-bead-blasted surfaces, for a contact pressure of 16 MPa.

First, in Fig. 5(a), the simulated pressure distribution in the contact plane is shown as a result of the mechanical simulation. It is evident that the two bodies are only in contact at discrete spots, which is due to surface roughness. The contact spots are evenly distributed over the surface, which is due to the isotropic height distribution of the surfaces. Fig. 5(b) shows the calculated resulting geometry of the contact of the bottom and top side, taking into account the elastic and plastic deformation due to the occurring pressure field. As in the pressure field, the macroscopically flat shape of the two surfaces shows the uniform distribution of the contacts and a similar size of the cavities. Fig. 5(c) shows the resulting measured and calculated temperature field on the front side of the samples ($y = 0\,\text{mm}$) near the contact plane. The simulated isotherms are nearly horizontal, consistent with the uniform contact distribution predicted by the mechanics. When comparing the two temperature fields, it is noticeable that the measured and simulated temperature fields match except for a few small deviations, which can be explained by noise due to measurement inaccuracies. For a better comparison of the measured and simulated temperatures, the two temperature fields are each averaged in the x-axis direction and are then shown as a line plot in Fig. 5(d). In both cases, almost linear temperature curves are observed in the two sample solids, which confirms the quasi-steady state. The gradient in measurement and simulation is also the same, which suggests that the heat flow in the samples is the same. A temperature jump is observed in the contact plane, which is caused by the microscopic contact resistance due to the surface roughness and the resulting smaller contact area. This is also the same in the measurement and in the simulation. From an examination of the contact geometry in Fig. 5(b), it is clearly visible that the contact points are evenly distributed over the contact surface. However, there are not so many contact points directly at the edge and therefore no good heat paths, which explains why the temperature profiles flatten out near the contact zone ($z = 0\,\text{mm}$). These comparisons validate the model for nominally flat, isotropic surfaces.

Next, the results for sample pairing no. 2 at a contact pressure of $p = 16\,\text{MPa}$ are shown in Fig. 6. In this pairing, the two surfaces have a macroscopic surface profile in addition to the microscopic surface roughness due to the milling process selected for manufacturing, so that the two samples are more elevated in the y-axis direction in the center than at the edge. The influence of this macroscopic unevenness on the mechanics and geometry of the contact is evident in the calculated pressure field in Fig. 6(a). There it is observed that the contact spots mainly form line contacts in the center of the sample ($y = 8 - 11\,\text{mm}$) and are therefore not so well distributed over the entire surface. The same is confirmed by a look at the resulting contact geometry in Fig. 6(b). In the measured temperature field on the front of the sample Fig. 6(c) it is also noticeable that the isotherms are almost horizontal in this case too. This is due to the fact that even if the contacts are not homogeneously distributed over the surface, they are still evenly distributed across the width. The simulation also shows the same behavior. The exact temperature profile is better visualized in the line plot in Fig. 6(d). Almost linear temperature profiles are observed in the solid material of both samples. The temperature gradient near the contact plane ($z = 0\,\text{mm}$) decreases, which is due to the macroscopic unevenness of the sample surfaces. As evident in the pressure profile in Fig. 6(a), there is no contact directly at the measuring surface ($y = 0\,\text{mm}$). This explains the decreasing gradient on the front side, as less heat can be transferred there than in the areas in the middle of the samples where there is contact. For this sample pairing, both a microscopic contact resistance due to the surface roughness and a macroscopic contact resistance due to the surface shape are present [14]. The temperature profile of the simulation shows good agreement with the measurement. This demonstrates that the model also captures contact heat transfer for surfaces with superimposed macroscopic form.

Finally, Fig. 7 shows the results for sample pairing no. 3 at a contact pressure of 16 MPa. Due to the macroscopic U-shaped unevenness of the lower sample, the pressure profile in Fig. 7(a) shows that only line contacts occur at the edges ($x = 0 - 1\,\text{mm}$ and $x = 19 - 20\,\text{mm}$) and there is no contact at all in the middle. This is confirmed by the diagram shown in Fig. 7(b), according to which the samples lie on top of each other at the edge while a distance of approx. $\Delta z = 60\,\mu\text{m}$ remains in the middle. However, after the experiment, contact marks were detected in the center of the upper sample. The only possible explanation for this is a lateral displacement of the macroscopic protrusions at the edges of the lower sample. In the resulting simulated temperature field at the front side in Fig. 7(c), the curved isotherms at the edges indicate that these are also the spots in the thermal model where most of the heat is transported. Comparing this with the infrared images, it is observed that the isotherms there run horizontally, suggesting a more uniform heat flow over the entire surface. While a temperature jump of approx. $\Delta T_c = 20\,\text{K}$ occurs in the simulation in the contact plane, this is significantly smaller in the measurement at approx. $\Delta T_c = 8\,\text{K}$. It is also noticeable that the temperature gradient in the upper and lower sample is significantly smaller in the simulation than in the measurement, which means that significantly more heat flows in the bodies in reality than the simulation states. This indicates that the

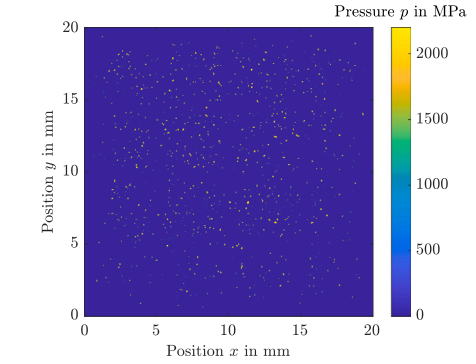

(a) Contact-pressure distribution.

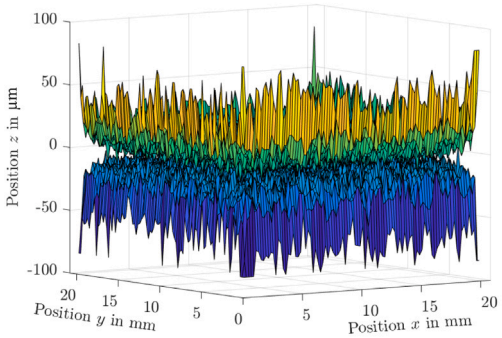

(b) Contact geometry.

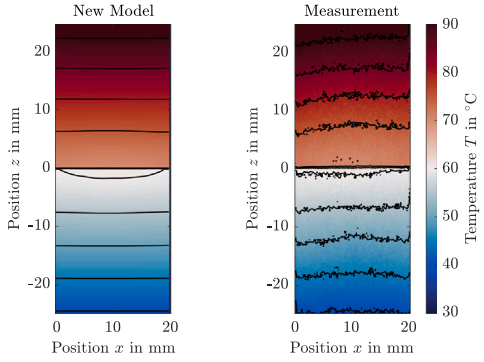

(c) Measured and simulated temperature field, along with isotherms, at $p = 16$ MPa at $y = 0$ mm. The values correspond to the respective ticks in the colorbar.

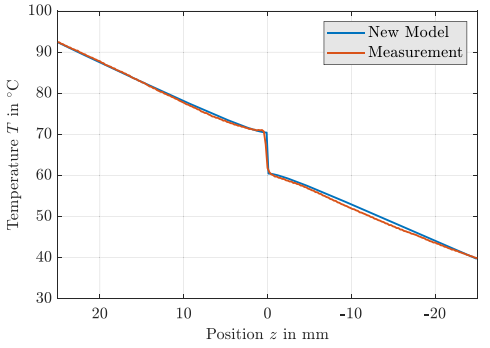

(d) Measured and simulated temperature profile at $p = 16$ MPa at $y = 0$ mm.

Fig. 5. Simulated and measured results compared for sample pairing no. 1 for a contact pressure of 16 MPa. Subfigures (a) and (b) present the mechanical simulation results, and (c) and (d) present the thermal simulation results.

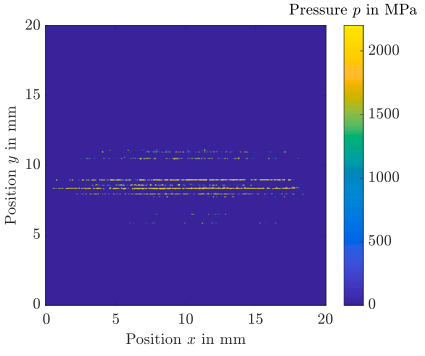

(a) Contact-pressure distribution.

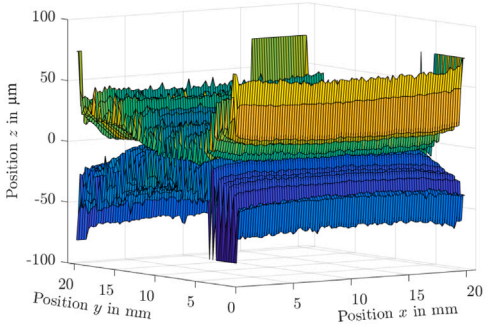

(b) Contact geometry.

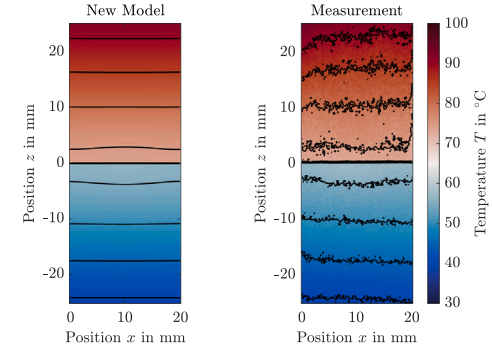

(c) Measured and simulated temperature field, along with isotherms, at $p = 16$ MPa at $y = 0$ mm. The values correspond to the respective ticks in the colorbar.

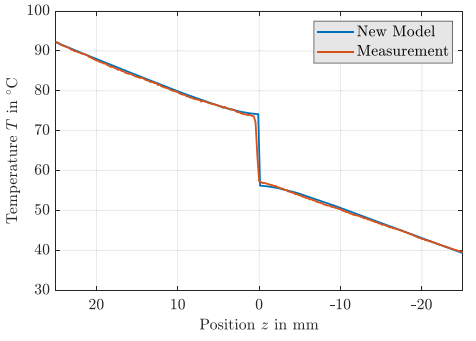

(d) Measured and simulated temperature profile at $y = 0$ mm.

Fig. 6. Simulated and measured results compared for sample pairing no. 2 for a contact pressure of 16 MPa. Subfigures (a) and (b) present the mechanical simulation results, and (c) and (d) present the thermal simulation results.

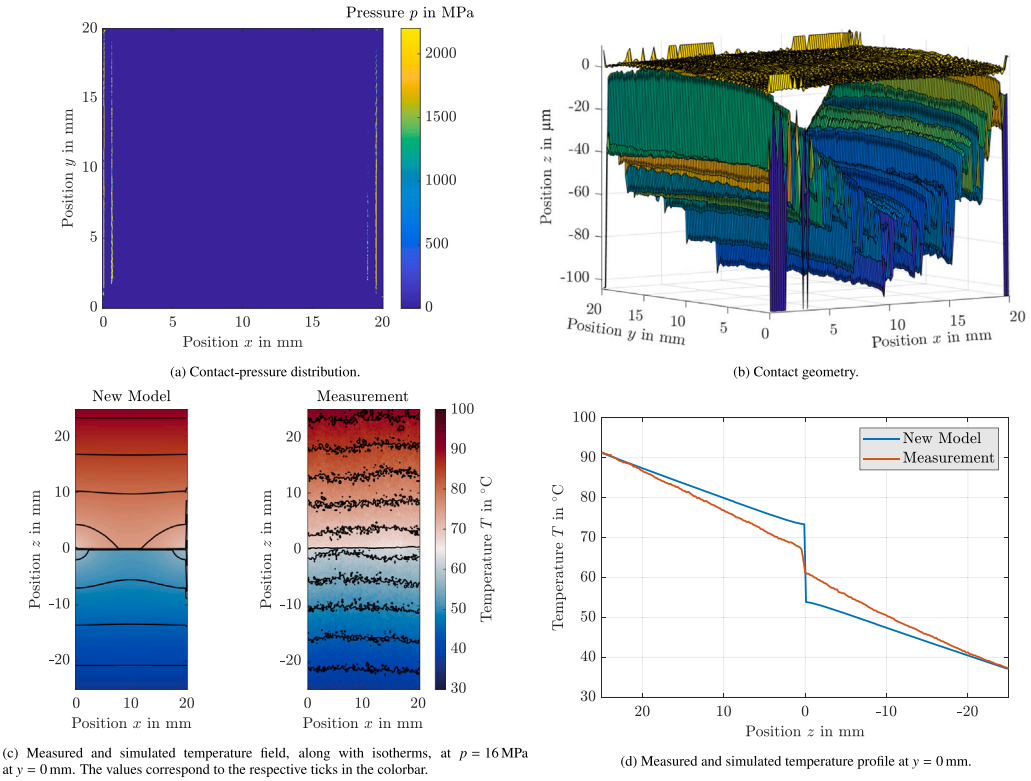

(a) Contact-pressure distribution.

(b) Contact geometry.

(c) Measured and simulated temperature field, along with isotherms, at $p = 16\,\mathrm{MPa}$ at $y = 0\,\mathrm{mm}$. The values correspond to the respective ticks in the colorbar.

(d) Measured and simulated temperature profile at $y = 0\,\mathrm{mm}$.

Fig. 7. Simulated and measured results compared for sample pairing no. 3 for a contact pressure of 16 MPa. Subfigures (a) and (b) present the mechanical simulation results, and (c) and (d) present the thermal simulation results.

thermal simulation was not set up with the correct geometric boundary conditions for this case. Consequently, the underlying mechanical half-space model does not capture the actual contact for this pairing. This is very likely due to the fact that only normal forces from linear displacements in the z-axis direction can be mapped in this half-space model and not tangential forces or displacements in the x or y-axis direction or torques. Due to the macroscopic shape of the surface of the lower specimen, however, displacements in the x-axis direction are to be expected there in particular. This highlights a limitation of the present mechanics and indicates that reliable prediction is expected for surface geometries where normal forces and normal displacements along the z-axis dominate [27].

5. Results

In the following, the contact heat transfer coefficient h_c for the two previously validated pairings no. 1 and no. 2 is determined as a function of the contact pressure p using the surface-resolved full-interface numerical model. To simplify the basis for calculating the contact heat transfer coefficient, heat loss at the outer surfaces of the samples to the ambient is neglected. In this way, the heat flow in z-direction remains constant in both samples and the contact heat transfer coefficient h_c can be determined simply via the series connection of thermal resistances assuming one-dimensional heat conduction, as shown in Eq. (13).

$$\dot{Q} = \left(\frac{1}{\frac{\Delta z_{\mathrm{sample,top}}}{\lambda} + \frac{1}{h_c} + \frac{\Delta z_{\mathrm{sample,bot}}}{\lambda}} \right) \cdot A_{\mathrm{nom}} \cdot \Delta T$$
$$h_c = \left(\frac{A_{\mathrm{nom}} \cdot \Delta T}{\dot{Q}} - \frac{\Delta z_{\mathrm{sample,top}} + \Delta z_{\mathrm{sample,bot}}}{\lambda} \right)^{-1} \tag{13}$$

It should be noted that the contact heat transfer coefficient h_c is quite sensitive to changes in the heat flow rate $\dot{Q}$, which is determined from the calculated 3D temperature field. When refining the grid, there is an interplay in the contact zone between cell sizes and contact geometry, which cannot be avoided. As a result, slight differences in the calculated temperature field might occur. These lead to slight changes in heat flow rate $\dot{Q}$, which in turn affects the contact heat transfer coefficient h_c. Thus, although the temperature RMSE is taken as the criterion for the determination of a sufficient grid resolution, as the temperature field is the result of the calculation, a remaining influence on the heat transfer coefficient cannot be avoided.

Fig. 8 shows the pressure-dependent contact heat transfer coefficients $h_c(p)$ determined using the new numerical method for the sample pairings no. 1 and no. 2 at a grid resolution of 768 × 768. As comparative values, the results of the old model by Frekers et al. [16] are shown for comparison. In this model, only a section of the surfaces of 2 × 2 mm in the middle of the sample surfaces is simulated with a grid resolution of 400 × 400. In addition, experimentally determined contact heat transfer coefficients are presented, which are obtained using an inverse evaluation method based on the temperature fields measured with the infrared camera introduced by Burghold et al. [17, 18]. For the experimental measurements, uncertainty is quantified via an inverse Monte Carlo analysis. The expanded uncertainties ($U = 2s$, $k = 2$) are listed in Table 3 and remain small across all pressures (no. 1: 2.63 - 3.13 %, no. 2: 0.87 - 1.76 %). This indicates robustness of the inverse estimation within the tested perturbation ranges. As a further comparison, the heat transfer coefficient determined empirically using the Mikić correlation is shown [11].

For sample pairing no. 1, a logarithmic profile for the contact heat transfer coefficient over pressure can be seen in all four curves. It is noticeable that the contact heat transfer coefficients determined with the new model are in strong agreement with the experimental results. The result from the Mikić correlation also shows a high degree of agreement with these two results. This is probably due to the fact that this correlation was developed precisely for a case with isotropic surface profiles. What is striking is that the slope of the empirical correlation is slightly larger than that of the numerical and experimental results.

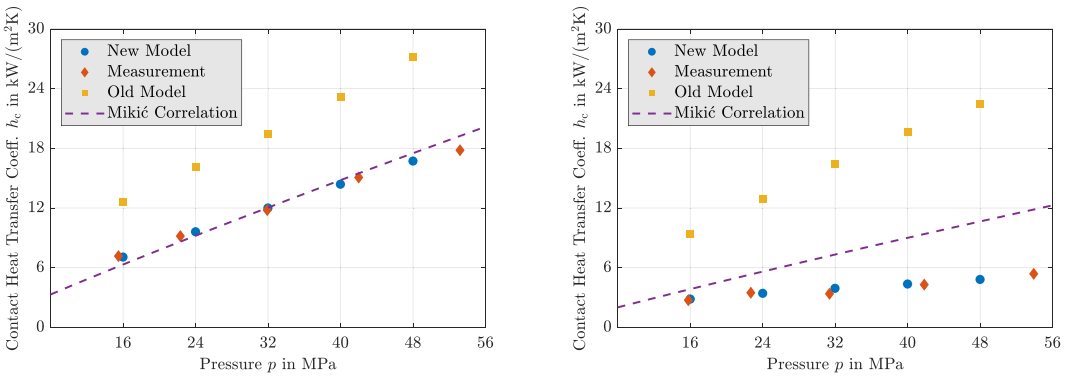

(a) Pairing no. 1. (b) Pairing no. 2.

Fig. 8. Comparison of calculated and measured contact heat transfer coefficients as a function of contact pressure.

Table 3
Inverse Monte–Carlo expanded uncertainties ($U = 2s, k = 2$) for the experimental h_c obtained by inverse evaluation at the tested contact pressures (pairings no. 1 and no. 2). Reference values $h_{c,\mathrm{ref}}$ are the unperturbed experimental inverse results.

Pairing	p in MPa	$h_{c,\mathrm{ref}}$ in W/(m^2 K)	U in W/(m^2 K)	$U/h_{c,\mathrm{ref}}$ in %
No. 1	15.5	7164	204	2.84
	22.3	9179	287	3.13
	31.9	11 789	331	2.81
	41.0	15 072	406	2.69
	53.2	17 813	468	2.63
No. 2	15.8	2738	48	1.76
	22.7	3481	50	1.43
	31.4	3374	52	1.54
	41.8	4297	40	0.92
	53.9	5383	47	0.87

This is due to the fact that the correlation assumes surfaces without macroscopic unevenness. However, the manufactured samples have a minimal macroscopic unevenness, which reduces the contact area. The values calculated by the old model of Frekers et al. [16] are higher than the other results. This is due to the fact that only the microscopic resistance due to roughness is considered in this model, as only a small segment of the surface is calculated. Since the sample pairing no. 1 has hardly any macroscopic surface shape, the deviation is quite small.

For sample pairing no. 2, the four curves again each have a logarithmic profile. Here too, the results of the new model are close to the experiments and show good agreement. The slope of the curve from Mikić's correlation is significantly higher than that of the other two. This makes it clear once again that this correlation can only be used to a limited extent for complex surface geometries, as this cannot be mapped with the two surface parameters of root mean square roughness and mean of absolute slope. This still works well for isotropic surfaces, but is much more difficult for structured surfaces. The results of the old model by Frekers et al. are significantly higher in this case, which is due to the more pronounced macroscopic unevenness of the samples. As a result, the effect of the macroscopic thermal resistance, which cannot be reproduced by this model, is much more pronounced here.

6. Conclusion

This paper presents a surface-resolved full-interface numerical model for the determination of contact heat transfer coefficients between two measured surfaces. The approach not only models the temperature distribution near the surface but also the distribution within the solid samples. This allows for a comprehensive analysis that accounts for microscopic contact resistance due to surface roughness and macroscopic contact resistance arising from long-wave surface shapes. Utilizing this model, it is possible to assess the contact area and geometry, as well as the resulting temperature field at the interface. The numerical model was validated against surface-temperature measurements obtained by infrared thermography. The temperature profiles from both the experiment and simulation show good agreement. A limitation of the mechanical model is its capability to represent only normal surface deformation during contact.

Using this model, the pressure-dependent contact heat transfer coefficient for each sample pairing can be derived based on the calculated temperature field. The results indicate that incorporating macroscopic resistance by modeling the entire sample surface improves the alignment of the determined heat transfer coefficients with experimental results compared to models that do not account for this factor. Future research will focus on advancing the mechanical model to better capture three-dimensional surface deformations, similar to finite element method (FEM) simulations, enabling validation across a broader range of surface geometries.

Nomenclature

Symbol	Quantity	Unit
a	Thermal diffusivity	mm^2/s
A	Area	m^2
C	Rigidity matrix	µm/MPa
E	Young's modulus	GPa
h_c	Contact heat transfer coefficient	W/(m^2 K)
H	Material hardness	MPa
m	Mean absolute slope	–
N	Number of surface elements	–
p	Contact pressure	MPa
$\dot{Q}$	Heat flow rate	W
T	Temperature	K
u_z	Overlap	µm
x, y, z	Coordinates	µm
z	Surface height (matrix)	µm
δ	Mean separation length	µm
ϵ	Emissivity	–
η, ξ	Local coordinates	µm
λ	Thermal conductivity	W/(m K)
ν	Poisson's ratio	–
σ	Std. dev. of profile height	µm
σ_y	Yield strength	MPa

CRediT authorship contribution statement

Tim Göttlich: Writing – original draft, Visualization, Validation, Investigation. **Mustafa Çavdır:** Visualization, Software, Methodology, Investigation. **Thorsten Helmig:** Supervision, Methodology, Conceptualization. **Reinhold Kneer:** Writing – review & editing, Supervision, Project administration, Funding acquisition.

Declaration of competing interest

The authors declare that they have no known competing financial interests or personal relationships that could have appeared to influence the work reported in this paper.

Acknowledgments

The authors thank the German Research Foundation (DFG) for funding the SFB/Transregio–96 collaborative research project "Thermo–energetic design of machine tools" project no. 174223256 (subproject T14). Furthermore, we would like to thank Florian Beyer for his support in validating the mechanical model and Eduard Weisser (Fraunhofer Institute for Laser Technology, RWTH Aachen University) for the white light interferometer surface scans of the sample test surfaces.

Data availability

Data will be made available on request.

References

[1] O. Wallscheid, Thermal monitoring of electric motors: State-of-the-art review and future challenges, IEEE Open J. Ind. Appl. 2 (2021) 204–223, http://dx.doi.org/10.1109/OJIA.2021.3091870.

[2] X. Zhang, Z. Li, L. Luo, Y. Fan, Z. Du, A review on thermal management of lithium-ion batteries for electric vehicles, Energy 238 (2022) 121652, http://dx.doi.org/10.1016/j.energy.2021.121652.

[3] K.E. Parmenter, E. Marschall, Influence of surface preparation on thermal contact conductance of stainless steel and aluminium, Exp. Heat Transf. 8 (3) (1995) 195–208, http://dx.doi.org/10.1080/08916159508946501.

[4] T. McWaid, E. Marschall, Thermal contact resistance across pressed metal contacts in a vacuum environment, Int. J. Heat Mass Transf. 35 (11) (1992) 2911–2920.

[5] A. Tariq, M. Asif, Experimental investigation of thermal contact conductance for nominally flat metallic contact, Heat Mass Transf. 52 (2) (2016) 291–307, http://dx.doi.org/10.1007/s00231-015-1551-1.

[6] Jeevanashankara, C.V. Madhusudana, M.B. Kulkarni, Thermal contact conductances of metallic contacts at low loads, Appl. Energy 35 (1990) 151–164.

[7] R. Dou, T. Ge, X. Liu, Z. Wen, Effects of contact pressure, interface temperature, and surface roughness on thermal contact conductance between stainless steel surfaces under atmosphere condition, Int. J. Heat Mass Transf. 94 (2016) 156–163, http://dx.doi.org/10.1016/j.ijheatmasstransfer.2015.11.069.

[8] A.M. Clausing, B.T. Chao, Thermal contact resistance in a vacuum environment, J. Heat Transf. (1965) 243–251.

[9] M.M. Yovanovich, Four decades of research on thermal contact, gap, and joint resistance in microelectronics, IEEE Trans. Components Packag. Technol. 28 (2) (2005) 182–206, http://dx.doi.org/10.1109/TCAPT.2005.848483.

[10] M.G. Cooper, B.B. Mikic, M.M. Yovanovich, Thermal contact conductance, Intnal J. Heat Mass Transf. (12) (1969) 279–300.

[11] B.B. Mikic, Thermal contact conductance; theoretical considerations, Int. J. Heat Mass Transf. (17) (1974) 205–214.

[12] M.V. Murashov, S.D. Panin, Numerical modelling of contact heat transfer problem with work hardened rough surfaces, Int. J. Heat Mass Transf. 90 (2015) 72–80, http://dx.doi.org/10.1016/j.ijheatmasstransfer.2015.06.024.

[13] B. An, L. An, Y. Huang, J. Li, B. Guan, R. Li, The influence of surface topography on thermal contact resistance of 7075-T6/beryllium bronze, Therm. Sci. Eng. Prog. 46 (2023) 102196, http://dx.doi.org/10.1016/j.tsep.2023.102196.

[14] M. Bahrami, J.R. Culham, M.M. Yovanovich, G.E. Schneider, Review of thermal joint resistance models for nonconforming rough surfaces, Appl. Mech. Rev. 59 (1) (2006) 1–12, http://dx.doi.org/10.1115/1.2110231.

[15] M.K. Thompson, Finite element modeling of multi-scale thermal contact resistance, in: Int. Conf. Micro/Nanscale Heat Transfer, 2008, pp. 509–517, http://dx.doi.org/10.1115/MNHT2008-52385.

[16] Y. Frekers, T. Helmig, E.M. Burghold, R. Kneer, A numerical approach for investigating thermal contact conductance, Int. J. Therm. Sci. 121 (2017) 45–54, http://dx.doi.org/10.1016/j.ijthermalsci.2017.06.026.

[17] E.M. Burghold, Y. Frekers, R. Kneer, Determination of time-dependent thermal contact conductance through IR-thermography, Int. J. Therm. Sci. 98 (2015) 148–155, http://dx.doi.org/10.1016/j.ijthermalsci.2015.07.009.

[18] E.M. Burghold, Y. Frekers, R. Kneer, Transient contact heat transfer measurements based on high-speed IR-thermography, Int. J. Therm. Sci. 115 (2017) 169–175, http://dx.doi.org/10.1016/j.ijthermalsci.2017.01.019.

[19] S. Chantasiriwan, Inverse determination of steady-state heat transfer coefficient, Int. Commun. Heat Mass Transf. 27 (8) (2000) 1155–1164, http://dx.doi.org/10.1016/S0735-1933(00)00202-5.

[20] M.N. Özisik, H.R.B. Orlande, Inverse Heat Transfer: Fundamentals and Applications, Routledge, 2000, http://dx.doi.org/10.1201/9780203749784.

[21] JCGM, Evaluation of measurement data — supplement 1 to the "guide to the expression of uncertainty in measurement" — propagation of distributions using a monte carlo method, 2008, http://dx.doi.org/10.59161/JCGM101-2008.

[22] D. Goerke, K. Willner, Normal contact of fractal surfaces—Experimental and numerical investigations, Wear 264 (7–8) (2008) 589–598, http://dx.doi.org/10.1016/j.wear.2007.05.004.

[23] F. Beyer, Numerische untersuchungen zur kontaktmechanik in der blechmassivumformung, in: Schriftenreihe Technische Mechanik, Lehrstuhl für Technische Mechanik, 2019.

[24] K. Willner, Kontinuums- und Kontaktmechanik: Synthetische und Analytische Darstellung, Springer-Verlag, Berlin, Heidelberg, 2003, http://dx.doi.org/10.1007/978-3-642-55814-6.

[25] H. Hencky, Über einige statisch bestimmte fälle des gleichgewichts in plastischen körpern, ZAMM - J. Appl. Math. Mech. / Zeitschrift Für Angew. Math. Mech. 3 (4) (1923) 241–251, http://dx.doi.org/10.1002/zamm.19230030401.

[26] C.Y. Poon, R.S. Sayles, Numerical contact model of a smooth ball on an anisotropic rough surface, J. Tribol. 116 (2) (1994) 194–201, http://dx.doi.org/10.1115/1.2927196.

[27] K. Willner, Fully coupled frictional contact using elastic halfspace theory, J. Tribol. 130 (3) (2008) http://dx.doi.org/10.1115/1.2913537.